scientific reports

OPEN

Quantitative microvessel orientation biomarkers derived from contrast free ultrasound imaging for cancer diagnosis

Pradeep Kumar Chaudhary[1], Nicholas B. Larson[2], Azra Alizad[1,3,4]✉ & Mostafa Fatemi[1,4]✉

Microvessel orientations are known to differ between benign and malignant tumors. This article introduces novel orientation-based quantitative biomarkers for contrast-free ultrasound microvasculature imaging to distinguish malignant from benign breast lesions. The proposed biomarkers were computed in both polar and Cartesian coordinates using images acquired by a high-definition microvasculature imaging technique. Seven biomarkers were derived based on the histogram, gradient angle, angle of penetration, and penetration factor of the microvessel. These biomarkers are first evaluated using simulated microvessel images and subsequently validated in in vivo studies on human breast masses. The new biomarkers demonstrated statistical significance in differentiating benign from malignant breast masses. In the in vivo study, the area under the receiver operating characteristic curve (AUC) for the proposed biomarkers was 0.91 (95% confidence interval [CI]: 0.86, 0.97). When the Breast Imaging Reporting and Data System (BI-RADS) score was included in the classification model, the AUC improved to 0.97 (95% CI: 0.91,1.00). These orientation-based biomarkers show promise in enhancing the diagnostic performance of ultrasound for classification of breast masses.

An increased tumor microvessel density is associated with an unfavorable outcome in invasive breast carcinoma, an angiogenesis-dependent malignancy[1]. Moreover, the microvessels in malignant tumors differ structurally from those in normal tissues or benign tumors. Low oxygen levels in early-evolving tumors trigger the secretion of vascular endothelial growth factors, promoting neovascularization and tumor progression[2]. The newly formed microvessels in malignant tumors are typically leaky, tortuous, irregular, and often oriented toward the center of the lesion[3]. In contrast, in most benign tumors, growth is regulated by mechanisms similar to those in normal tissue, leading to the formation of regularly shaped, non-tortuous vessels that are circumferentially oriented around the tumor[4]. Furthermore, microvessel patterns, such as vessel orientation, are important. Studies have reported that the presence of intratumoral penetrating vessels can predict breast malignancy[5,6]. However, these assessments have primarily relied on visual inspection. Therefore, quantifying orientation-based features of tumor microvessels offers the opportunity for more accurate and objective differentiation between benign and malignant tumors.

The traditional color Doppler is only sensitive to rapid flows, which limits its ability to study the structural details of microvessels effectively[6–8]. Clinical studies using contrast-enhanced ultrasonography[9,10] as well as preclinical studies using acoustic angiography and ultrasonic localization microscopy with the use of contrast agents have been used for imaging microvessels[11–13]. Fine vascular features have been extracted at a super-resolution scale in spontaneous mouse models of breast cancer[14] and in humans[15] but the technique involves the injection of contrast agents, which makes it inconvenient and costly. High-frame-rate ultrasound with clutter removal processing has enabled Doppler imaging to visualize tumor microvessels without the need for contrast agents[16–18]. While superb microvessel imaging has been applied for the classification of breast masses, its quantification is limited to pixel counting and visual inspection[19]. Our research group developed a framework called quantitative high-definition microvasculature imaging (qHDMI), which visualizes tumor microvessels as small as 150 μm in diameter without contrast agents[18]. qHDMI extracts and quantifies vessel morphology for

[1]Department of Physiology and Biomedical Engineering, Mayo Clinic College of Medicine and Science, Rochester, MN 55905, USA. [2]Department of Quantitative Health Sciences, Mayo Clinic College of Medicine and Science, Rochester, MN 55905, USA. [3]Department of Radiology, Mayo Clinic College of Medicine and Science, Rochester, MN 55905, USA. [4]Azra Alizad and Mostafa Fatemi share senior authorship. ✉email: Alizad.azra@mayo.edu; fatemi.mostafa@mayo.edu

tumor classification across various organs[20,21]. The efficacy of qHDMI for diagnosing cancer lesions has been demonstrated in the breast[22], thyroid[23], liver[24], axillary lymph nodes[25], and the eye[26]. These studies focused on the morphological features, including density, shape, tortuosity, complexity, and irregularity patterns of tumor microvessels[20,21]. However, the orientation or directionality of microvessels was not included in their quantification. Studies utilizing conventional power Doppler[6] superb microvessel imaging[27] and Angio-plus[28–30] ultrasound techniques reported vessel distribution and orientation to differentiate breast masses. However, their methods were limited to qualitative and visual evaluation of vessels.

In this paper, we introduce a set of new quantitative biomarkers based on the orientation of tumor microvessels. We propose a new processing framework that utilizes two-dimensional HDMI images to measure orientation-based biomarkers. Using a synthetic dataset, first, we describe how the proposed method quantifies the circumferential and penetrating patterns. Then, we investigate the potential utility of these orientation-based biomarkers in classifying breast masses in vivo. We anticipate that this study can set a new set of angiogenesis-based imaging biomarkers for cancer diagnosis.

Methods

In the present study, we introduce new biomarkers to quantify orientation-based features of tumor microvessels in contrast-free ultrasound microvasculature images for classification of breast masses. These biomarkers comprise Cartesian coordinate features, including angle-based penetration density and penetration to circumferential density, as well as polar coordinate features, including histogram features and polar gradient angle. Simulation and in vivo studies were conducted to validate the proposed method.

Cartesian coordinate features

Penetrating microvessels are vessels that enter from the boundaries of the region of interest (ROI) and move toward its center. In contrast, circumferential microvessels may also enter the ROI through its boundaries but travel along the periphery rather than moving inward. Microvasculature image features in the conventional Cartesian coordinate can provide valuable quantitative information for lesion classification. Here, we quantify the orientation of microvessels based on the entry angle into the ROI, their entry location, and the penetration length within the ROI.

Angle-based penetration density (APD)
The proposed framework for computing the penetration density in Cartesian coordinates is illustrated in Fig. 1a. The objective is to determine whether the microvessels entering the ROI are penetrating inward or are circumferentially oriented around the ROI's periphery. To achieve this, we begin by identifying microvessel segments using connected component analysis. Connected component analysis is a segmentation operation used to isolate and label distinct regions in a microvessel, including the main trunk and its branches. It groups neighboring pixels based on connectivity, considering horizontal, vertical, and diagonal adjacency in 8 possible directions. Figure 1a illustrates two microvessel segments that are identified as connected component 1 (penetrating microvessel segment) and connected component 2 (circumferential microvessel segment). Among all the identified microvessel segments or connected components, only those that intersect with the ROI boundary are considered, i.e., the microvessel segment that shares one or more pixels with the ROI. Next, the angle between the two lines, the tangent to the ROI boundary at the entry point of the selected microvessel, and the line describing the direction of the microvessel are calculated. This angle can be calculated based on the slope of both lines. The mathematical expression for the angle is as follows.

$$\theta = tan^{-1}\frac{m2 - m1}{1 - (m2 \times m1)} \tag{1}$$

where, $m1$ is the slope representing the direction of the microvessel, and is the slope of the line tangent to the ROI boundary. To estimate $m2$, the tangent line is determined using the first ten boundary points of the ROI around the entry point. This way we can determine the tangent even for a non-circular ROI. The following steps outline how to compute the slope $m1$ of the microvessel:

1) Skeletonization: Extract the skeleton of the microvessel to achieve a single-pixel-wide representation of the microvessel while preserving its structure. This is accomplished using the morphological thinning algorithm, which iteratively removes pixels until only the central skeletal structure remains[31]

2) Endpoint and Branch Point Identification: Obtain the endpoints, i.e., identify pixels on the skeleton that have exactly one neighboring pixel; Obtain the branch points, i.e., identify pixels with more than two neighboring pixels.

3) Branch Isolation: Remove the branch points identified in step 2 to isolate the individual branch from the skeleton, resulting in disconnected branches.

4) Branch Slope Estimation: Fit a straight line to each disconnected branch using a curve fitting algorithm and record the slope and intercept.

5) ROI Contact Branch Identification: Identify the branch that contacts the ROI boundary by finding a branch sharing a point with the boundary. Then, the slope and intercept of this branch are used as initial conditions for the estimation of the final line fitted to the microvessel. In cases where a microvessel segment has multiple entry points, the first contact point during a left-to-right scan will be considered as the point of contact.

6) Final Line Fitting: Fit a line to the binary microvessel coordinates ($Microvessel_x$, $Microvessel_y$), under the following two constraints: (a) The line must originate at a contact point ($Intersect_x$, $Intersect_y$), where the initial branch intersects the ROI boundary. (b) The slope of the line must lie within the range
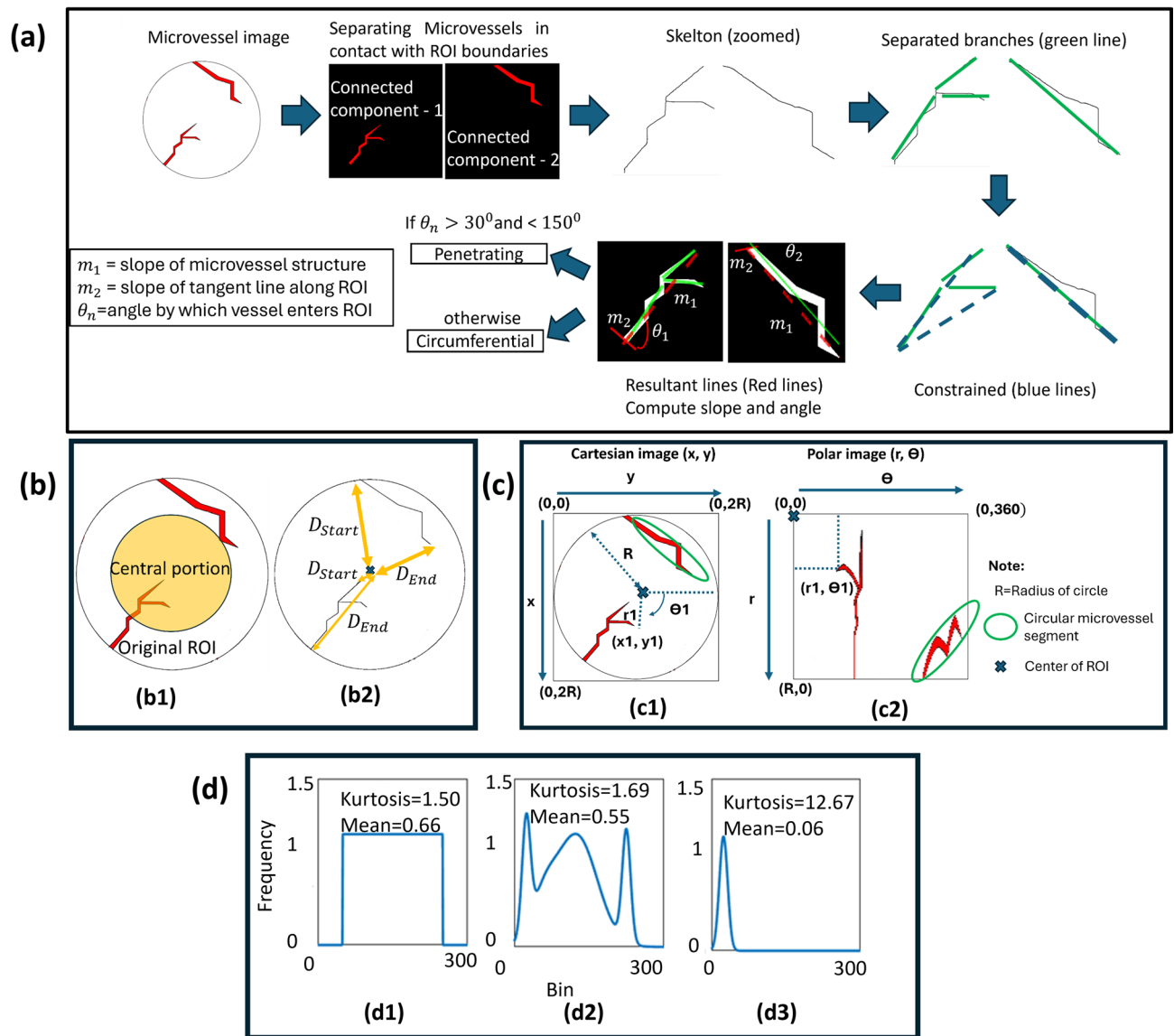
Fig. 1. Orientation biomarker method illustration. (**a**) Framework categorizing penetrating and circumferential microvessels for computing angle based penitartion density (APD). (**b**) Penitration to circumfrantial density (PCD) biomarker computation illustration: (**b1**) region of interest (ROI) and central portion (**b2**) Penitration length calculation. (**c**) Cartesian coordinate to polar coordinate conversion (Symbol X represents the center of the circle and green curve encloses circumfratial microvessl in both coordinate images). (**d**) Histogram-based biomarkers explanation: (**d1**) Flat distribution, (**d2**) Irregular and density distribution, and (**d3**) Peaky distribution.

defined by the minimum and maximum slopes [$m1_{min}$, $m1_{max}$] of all isolated branches. Finally, optimize the slope $m1$ that minimizes the mean squared error (MSE) function, defined as:

$$MSE(m1) = \sum (Microvessel_y - (m1 \times Microvessel_x, +(Inter \sec t_y - m1 \times Inter \sec t_x))$$

Such that: $m1_{min} \leq m1 \leq m1_{max}$

Then, we estimate the angle between the slopes $m1$ and $m2$. If the angle is between $30°$ and $150°$, we classify the microvessel as penetrating; otherwise, it is considered circumferential. Ideally, the angle range for a circular ROI should be between $45°$ and $150°$ for circular ROI. However, due to the irregular shape of the ROI, this range ($30°$ and $150°$) was determined using a trial-and-error approach. The study to determine the optimal ranges of angles is presented in the supplementary file section S1. To quantify the penetrating microvessels, we calculate the area Penetration Density (APD), defined as the ratio of the penetrating microvessels' area to the

total microvessel area. The area of binary images of microvessel segments can simply be computed by summing the number of pixels corresponding to each region.

Penetration to circumferential density (PCD)

In this approach, all the microvessels are first categorized into two groups: small microvessels and large microvessels. Small microvessels are defined as those whose skeleton length (SL) is less than 50 pixels. The small microvessels are not excluded from the analysis but are omitted from orientation-based classification due to the unreliability of their directional measurements. Microvessels in the large group are categorized into either penetrating or circumferential. A large microvessel is considered penetrating if the skeleton of the microvessel has a significant length and approaches the central region of the ROI. The central region of the ROI is determined by scaling down the original ROI to 70% of its size, as shown in Fig. 1b1. The central region of the ROI is obtained by first computing the ROI's centroid by estimating center of mass of it[32]. Then, the ROI is approximated with a polygon. Each vertex's distance from the centroid is then scaled by a fixed factor of 0.7, effectively shrinking the ROI uniformly toward its center. This method ensures a uniform scaling of the core shape of the ROI while minimizing edge effects, resulting in a smooth approximation. The illustration in Fig. 1b2 explains the concept of calculating the penetration length (PL) of a microvessel. The plus sign (+) marks the center point of ROI, while the irregular white line represents the skeleton of the microvessel segments 1 and 2. The PL is calculated as the absolute difference between the distances from the vessel skeleton's start and end points to the ROI center, (D_{start}) and (D_{End}), respectively. Mathematically, this is expressed as:

$$PL = |D_{start} - D_{End}|$$

In Fig. 1b2, the first coordinate point of the skeleton of either microvessel segment 1 or 2, identified (scanning from left to right and top to bottom pixels in Cartesian coordinates) is used for D_{Start}, while the last coordinate point determines D_{End}. Each microvessel segment will be analyzed individually. When PL = 0, it implies $D_{start} = D_{End}$, indicating a circumferential vessel. Conversely, PL = SL signifies that the microvessel is radial. Figure 1b2 shows a case where PL ≈ SL (microvessel segment or connected component1) and a case where PL ≈ 0, i.e., $D_{start} \approx D_{End}$ (microvessel segment or connected component-2). To classify microvessels as penetrating, we introduce the penetration factor (PF), defined as PF = PL/SL. For our study, we set PF = 0.7, meaning microvessels with PL > 0.7SL are considered penetrating, while others are classified as circumferential. The selection process for PF and the central region area is detailed in the supplementary file section S2.

Additionally, small microvessels and other larger vessels with low PL are considered penetrating if a portion of them lies within the central region of the ROI. This criterion ensures that only microvessels that are in the center of the ROI are classified as penetrating; otherwise, they are categorized as circumferential. Finally, the Penetration-to-Circumferential Density (PCD) is defined as the ratio of the area of penetrating microvessels to that of circumferential microvessel.

The primary distinction between APD and PCD lies in how they characterize penetrating and circumferential microvessels. APD characterizes microvessel segments based on their entry angle into the ROI, but it only considers those that directly contact it. This approach may overlook discontinuous microvessels due to the limitations of 2D lesion imaging in capturing a 3D structure. In contrast, PCD accounts for all microvessel segments, providing a more complete measure of penetration density. Together, APD and PCD provide complementary insights; APD offers an angular perspective, while PCD assesses penetration level more.

Polar image features

To define additional parameters, we need to convert the image from a Cartesian to a polar coordinate. The conversion from Cartesian (x, y) to polar coordinates (r, θ), where $r = \sqrt{(x^2 + y^2)}$ and $\theta = \tan^{-1}(y/x)$.

Here, r represents radial distance, varying from 0 to R, where R is half of the maximum diameter of the ROI in Cartesian coordinates. R can also be defined as the radius of the smallest circle that encompasses the entire ROI. For illustration purposes, Fig. 1c1 depicts a Cartesian image consisting of a circular-shaped ROI. The microvessel segments 1 and 2 within ROI represent a penetrating and a circumferential microvessel, respectively. Figure 1c2 demonstrates the converted polar image. The penetrating microvessel segment in the Cartesian image is seen as a vertical microvessel segment in the polar image; on the other hand, the circumferential microvessel appears as a horizontal microvessel segment in the polar image. The ($r1$, $\theta 1$) in Fig. 1 c represent a point in both polar planes which corresponds to point (x1, y1) in the Cartesian plane. Four histogram features and the gradient angle are computed from the image converted to polar coordinates.

Histogram features

A histogram converts a binary polar image matrix into a vector, where each index corresponds to either the radius (r) or the angle (θ). The radius r ranges from 0 to R, while the angle θ range from $0°$ to $360°$. A radial histogram is derived when the horizontal axis of the plot represents r, and the vertical axis represents the number of pixels at each r. Conversely, a tangential histogram is obtained when the horizontal axis represents θ, and the vertical axis represents the number of pixels at each θ. The mean radial histogram (MRH) and mean tangential histogram (MTH) represent the average distribution of microvessels along the radial and tangential directions, respectively. Simply put, they indicate the density of microvessels in these directions. Kurtosis of these histograms indicates the peakedness of the microvessel distribution in these directions[33]. A high kurtosis indicates a tall, narrow peak with localized clustering of microvessels and potentially lower mean density, while low kurtosis indicates a flatter distribution, i.e., more uniform distribution. Figures 1(d1), (d2), and (d3) illustrate examples of variation in kurtosis and mean values of flat, irregularly densely distributed, and peaky distribution histograms. When microvessels are highly dense and evenly distributed throughout the ROI, the radial histogram tends

to be flat or irregularly dense. Conversely, if microvessels are concentrated along the circumferential region or radiating toward the ROI, the radial or tangential histogram will appear peaked, respectively. Thus, depending on the orientation and density of the microvessel, the kurtosis and mean distribution of the histogram will vary. Consequently, all four features: MRH, MTH, Kurtosis$_r$(kurtosis of radial histogram), and Kurtosis$_\theta$ (kurtosis of the tangential histogram) are critical for quantifying the orientation of microvessels within the ROI.

Polar gradient angle (PGA)
The radial and tangential gradients correspond to the changes in pixel intensities along the vertical and horizontal directions of the skeleton image in polar coordinates. The skeleton image is obtained by iteratively thinning the binary polar image until only the central single-pixel-wide structure remains. The Prewitt kernel of size 3×3 (A=[1,1,1;0,0,0;-1,-1,-1]) is used to compute the gradient matrix G_θ and G_r by convolving the A and its transpose with the skeleton image. Since the gradient angle is computed on the skeleton, the choice of kernel is not consequential. After computing G_θ and G_r, the angle θ at each pixel can be computed using the expression $\tan^{-1}(G_r/G_\theta)$. First, the mean of the gradient angle (MGA) of the ith skeleton (corresponding to i^{th} microvessel segment) is computed. Then, the weighted mean of all N microvessel segments is calculated to obtain PGA, where the weight is based on the area of each microvessel segment in Cartesian coordinates. The weight will give greater importance to segments with larger area. This approach is desirable, as larger microvessels tend to dominate in the lesion. The mathematical expression for PGA is as follows

$$PGA = \left| \frac{\sum_{i=1}^{N} (W_i \times MGA_i)}{\sum_{i=1}^{N} W_i} \right| \tag{2}$$

where W_i and MGA_i represent the area and MGA of ith microvessel segment, respectively.

Simulation study
To illustrate the biomarkers and methods for quantifying circumferential and penetrating microvessels, we utilized AutoCAD® 2024 to design microvessel structures within circular lesions. Five cases were created: three featuring simple microvessel structures and one showcasing a complex structure characterized by tortuous patterns and branching microvessels. The four cases of microvessel structures are as follows: (1) dominant circumferential microvessels, (2) dominant penetrating microvessels, and (3) a combination of both circumferential and penetrating microvessels (incorporating features of case 1 and case 2), (4) four complex microvessel structures, with two featuring circumferential microvessels, and the other two presenting penetrating microvessels, and (5) low-resolution version of case 4 was generated by first introducing salt-and-pepper noise (5% noise density) to the image, then downsampling it by 95% to lose information, and finally upsampling it back. The first row of Fig. 2 illustrates the microvessel network for all four cases. Cases 1, 2, and 3 share common microvessel patterns labeled as MV1, MV2, MV3, and MV4, where MV1 and MV4 represent circumferential microvessels, and MV2 and MV3 represent penetrating microvessels. In contrast, cases 4 and 5 include four complex structures labeled as CMV1, CMV2, CMV3, and CMV4, where CMV1 and CMV4 represent circumferential and CMV2 and CMV3 represent penetrating microvessel segments. The second row of Fig. 2 shows the microvessel structure in polar coordinates, and the subsequent rows illustrate and display the biomarker values.

The radial histogram is found to be distributed over a wide range of r in the case where only radial microvessel structure is present, whereas the histogram shows peaks when only circumferential microvessels are present. So, for circumferential-only distribution (case 1), a high value of kurtosis$_r$ and a low value of MRH is observed compared to the penetrating-only case (case 2) and the combination of both microvessel structure types (cases 3, 4 and 5). Therefore, MRH and kurtosis$_r$ will be able to distinguish lesions having only circumferential microvessels from those having a combination of circumferential and penetrating microvessels or having only penetrating microvessels. For the tangential histogram, peaks in the distribution are observed when there are only penetrating microvessels (case 2), which is shown by high kurtosis$_\theta$ and low MTH values compared to the only circumferential and the mixed microvessel orientation structures. Another key point to note is that, for the penetrating microvessels, kurtosis$_\theta$ will be much higher than kurtosis$_r$, whereas the opposite is true for the circumferential microvessel pattern. In lesions exhibiting both types of microvessel structures, kurtosis will not be helpful, however, a high MRH or high MTH or both MRH and MTH can provide valuable insights. PGA was found to be low for structures having only circumferential microvessels, moderate for structures having mixed distribution, and high for only penetrating microvessel structures. In the APD row of Fig. 2, the long black lines represent the curve-fitted lines to the microvessels, while the short black lines represent tangents to the circular ROI, all obtained using the proposed method. The values of APD were found to be zero for the circumferential-only structure, one for the penetrating-only microvessel structure, near zero for the dominating circumferential microvessel structure, and above 0.5 for the dominating penetrating microvessel structure. In the PCD row, two images are shown for each case to illustrate the penetrating and circumferential microvessel structures. In these images, the blue region highlights the ROI, while the brown region represents the central ROI, which is a scaled-down version of the ROI (scaled by a factor of 0.7). The PF value is found to be low for circumferential microvessel structures (MV1, MV4, CMV3, and CMV4) and high for penetrating microvessel structures (MV2, MV3, CMV1, and CMV2). A microvessel structure is characterized as penetrating in the PCD approach if it has a high PF and is also contained within the central ROI (brown region). The PCD values are found to be zero for purely circumferential microvessels, very high for purely penetrating microvessels, less than 1 for predominantly circumferential microvessels, and greater than 1 for predominantly penetrating microvessel structures. Case 4 shows a complex structure characterized by branching and tortuous patterns. The histogram pattern reflects a dominating penetrating nature, as evidenced by the high MRH and MTH values, indicating a
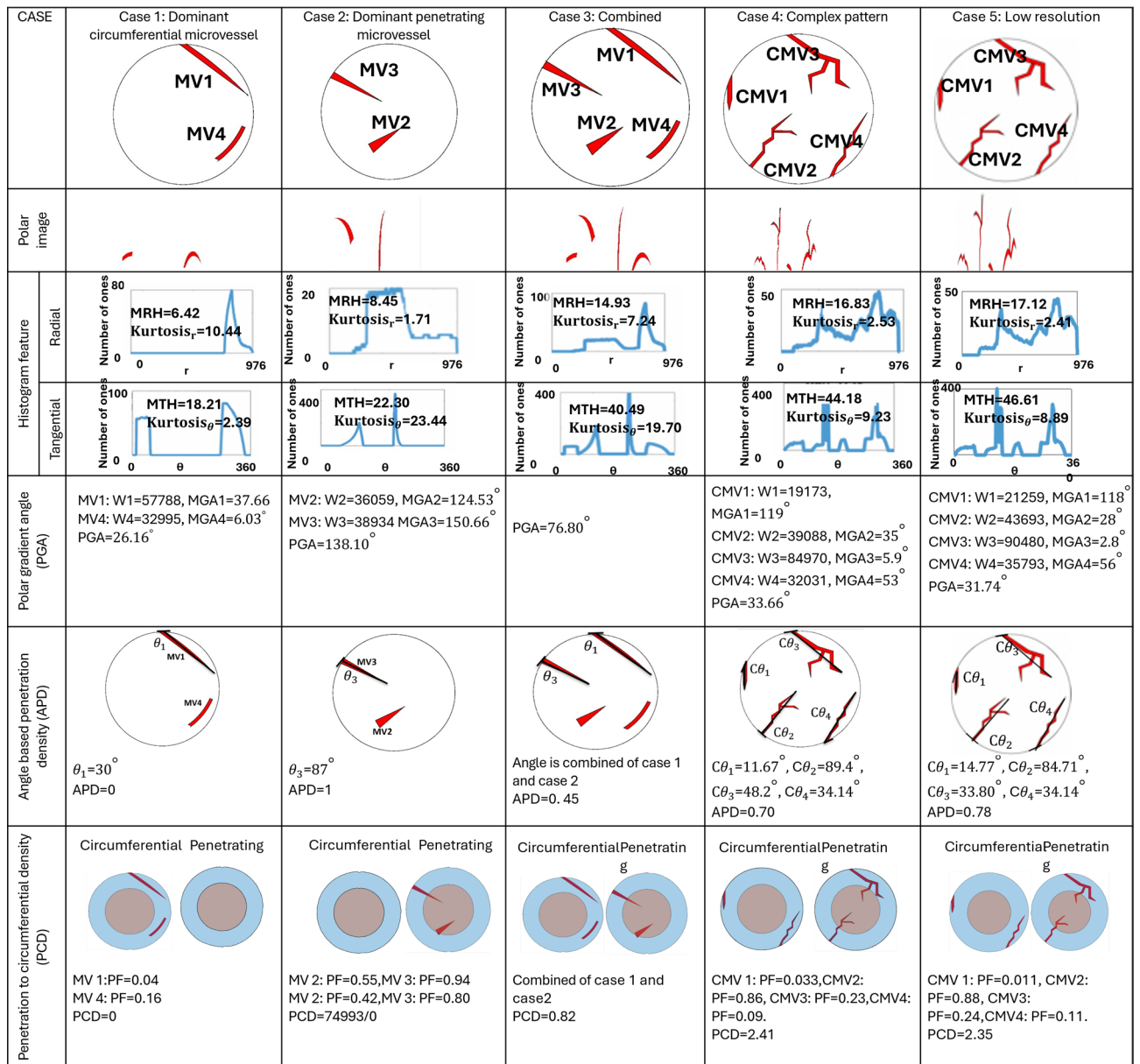
Fig. 2. Results of simulation study. Row 1: Microvessel structures for cases 1, 2, 3, 4, and 5. MV1, MV2, MV3, and MV4 are labels of microvessel structure, and CMV1, CMV2, CMV3, and CMV4 labels complex microvessel structure. Row 2: Microvessel structures of all four cases in polar coordinates. Row 3: radial and tangential histogram plots with the biomarker values, biomarkers MRH, kurtosis_r, MTH, and kurtosis_θ. Row 4: Weight (W) and mean gradient angle (MGA) values for each microvessel structure, along with the PGA values, are shown for each case. Row 5 illustrates the approach used to compute the angle $\left(\theta_i \text{ and } C\theta_i\right)$ for i^{th} simple and complex microvessel structure in contact with ROI along with APD values for each case. Finally, Row 6: illustrate circumferential and penetrating microvessel structures derived using the PCD approach, along with the values of penetration factor (PF) of each microvessel structure inside lesion and PCD values corresponding to each case.

dense distribution of microvessels in both radial and tangential directions. The significantly higher kurtosis_θ compared to kurtosis_r suggests a more uniform distribution of microvessels along the radial direction than the tangential direction, implying a stronger penetrating pattern than a circumferential one. The PGA value is near the middle of the angular range that spans from circumferential (0°) to penetrating (180°) patterns, suggesting characteristics of both microvessel types. Additionally, an APD value exceeding 0.5 and a PCD value greater than 1 further indicate the predominance of a penetrating pattern over the circumferential one. The effect of number of branches on biomarker values depends on the microvessel segment type. In circumferential microvessels, an increase in branches leads to decrease in PCD and APD. Meanwhile, MRH and MTH values increase, with MTH exhibiting a proportionally greater rise. The value of kurtosis_θ and kurtosis_r decrease due to reduced

sparsity in both directions. PGA also decreases, though this may vary depending on branch weight and pattern. Similarly, in penetrating microvessel segments, a comparable trend is observed in histogram features, but MRH increases proportionally more. The value of kurtosis_θ and kurtosis_r decrease (due to reduced sparsity), with kurtosis_θ remain higher than kurtosis_r (i.e., more uniform distribution in radial direction). Conversely, PGA, APD, and PCD values increase as the area of penetrating microvessel segments increases. To evaluate the effect of noisy images, Case 5 has been included in the simulation study to assess the percentage difference in the biomarker values for low-resolution noisy images. We observed that a 95% decrease in resolution resulted in +1.7%, +5.5%, -4.7%, -3.6%, -5.7%, +10.2%, and -2.4%, for MRH, MTH, kurtosis_r, kurtosis_θ , PGA, APD, and PCD, respectively. A higher error was observed in APD, likely due to the blurring effect caused by downscaling. However, it's important to note that despite the low-resolution, the biomarkers seem robust. Additional analysis was conducted to assess the sensitivity of MTH and MRH to minor shift or translation in ROI (±15 pixels in both the x- and y-directions). The maximum observed percentage change was approximately 1.6% (see supplementary section S3).

In vivo study

This study included a total of 70 subjects, each having at least a single ultrasound-identifiable breast lesion, mostly classified as BI-RADS 4 and up, and recommended for core needle breast biopsy. The study was Health Insurance Portability and Accountability Act–compliant and approved by the Institutional Review Board (IRB). Signed IRB-approved written informed consent with permission for publication was obtained from each participant before enrollment. Details about the study subjects are summarized in Table 1. Following the ultrasound examination, core needle breast biopsies were performed on all patients, and the pathology reports were used to make the final diagnosis.

Image acquisition and processing

In vivo images of breast tumor microvessels were acquired using the high-definition microvessel imaging (HDMI) method[18]. An Alpinion ultrasound system, Ecube12-R (ALPINION Medical Systems, Seoul, South Korea), equipped with a linear array running at 8.5 MHz, L3-12 H (ALPINION Medical Systems), was used to acquire the images[20].

Microvessel image formation includes the following steps. First, plane-wave imaging mode was employed to identify the breast mass in the B-mode image. The R01 is marked by an expert sonographer on the plane-wave B-mode image during acquisition. Subsequently, a series (~ 2000) of high-frame-rate images at 600 frames per second are captured at each tumor site, where each frame is formed using 5-angle coherent plane-wave compounding. After applying singular value decomposition (SVD) processing, background noise is removed, and vessel enhancement filtering is performed. This results in the final HDMI image of the tumor microvessels. Then, through a series of morphological filtering and vessel segmentation, we convert the HDMI image into a binary image, identify the skeleton, and extract the vessel segments[21]. Figure 3 illustrates the steps involved in obtaining HDMI images of a breast tumor.

Statistical analysis methods

For the in vivo study, the distributional differences between malignant and benign lesions were tested using the Wilcoxon rank-sum test. The hypothesis was tested using a two-sided alternative, and the p-values for each biomarker were adjusted based on the Holm-Šídák method. Biomarker discrimination was assessed based on receiver operating characteristic (ROC) curve analysis, where the area under the ROC curve (AUC) and 95% confidence intervals (CIs) were estimated using bootstrapping. Classification measures, including sensitivity (SEN) and specificity (SPE) were estimated based on the Youden index. Threshold optimization was applied to obtain out-of-bag bootstrap estimates and corresponding 95% CIs, reducing bias from data-driven threshold selection. Correlation among biomarkers was evaluated using the Pearson correlation coefficient.

Multivariable logistic regression was used to evaluate the collective classification performance of various combinations of biomarkers, including radial histogram features, tangential histogram features, polar coordinate features, Cartesian coordinate features, the proposed seven biomarkers, and the proposed biomarkers combined with BI-RADS. To address overfitting due to the small sample size, principal component analysis (PCA) was applied for dimension reduction, and the leading principal components were used for model fitting. Model performance was assessed in a manner consistent with the evaluation of individual biomarkers. All bootstrapping

Lesion	Benign	Malignant
Number of subjects	35	35
Age (mean ± Standard deviation)	50 Years	60.6±13.7 Years
Lesion Size (mean ± Standard deviation)	14.2±8.3 mm	18.82±11.4 mm
BIRADS (count and percentage)	3 (count=4, Percentage =11.4%)	4 (count=16, Percentage =45.7%)
	4 (count=30, Percentage =85.7%)	5 (count=19, Percentage =54.2%)
	5 (Number=1, Percentage =0.02%)	

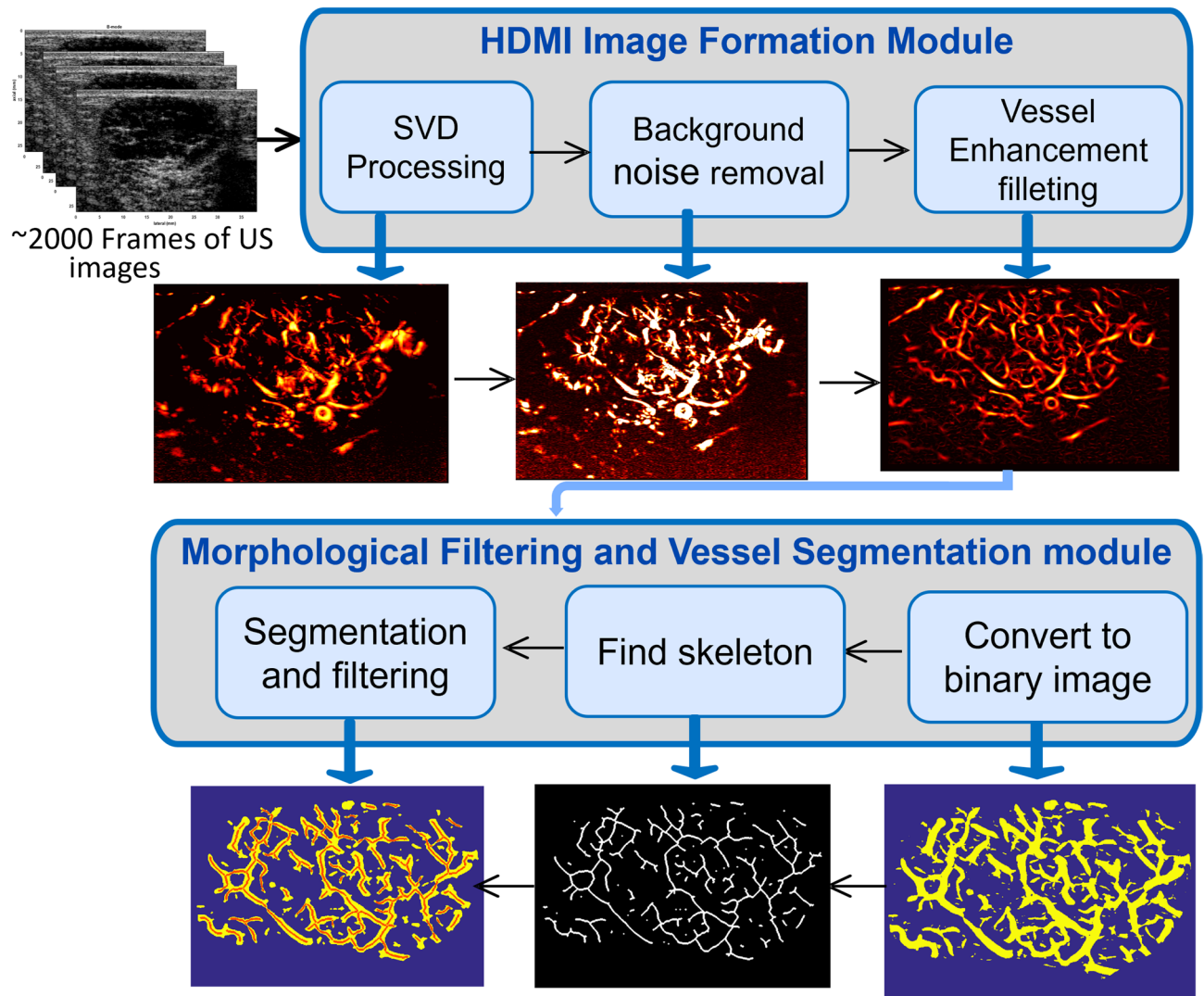**Table 1**. Summary of subject clinical characteristics.

Fig. 3. Schematic diagram of the HDMI image processing pipeline. A sequence of high-frame-rate ultrasound (US) data is acquired. Following clutter removal using singular value decomposition (SVD), background noise is suppressed, and vessel enhancement filtering is applied to generate the final HDMI image[18]. The Morphological Filtering and Vessel Segmentation Module then converts the enhanced image into a binary format, extracts the vessel skeleton, and identifies individual vessel structures that are prepared for quantification[21].

was performed using 1000 bootstrap samples, and reported CIs were derived using the quantile method. Statistical analyses were performed using R v. 4.3.1 (R Core Team, Vienna, Austria).

During the classification analysis, features are post-processed to consistently handle infinity (Inf) and not-a-number (NaN) values across all data, regardless of lesion type. NaN values occur when the microvessel image lacks any circumferential and penetration microvessels, leading to structural missingness. In such cases, NaN is replaced with zero, accurately reflecting the absence accurately reflects the absence of microvessel structures in the APD and PCD biomarkers. For the features $kurtosis_r$ and $kurtosis_\theta$, replacing NaN with zero does not imply missingness, as a kurtosis value of zero corresponds to a uniform distribution. This can occur in both benign and malignant lesions. The values of MRH and MTH, which become zero when structural elements are missing, serve as weighting variables for the zero values in $kurtosis_r$ and $kurtosis_\theta$ aiding in the differentiation of lesion types during analysis. Infinity values occur when a denominator is zero, such as when no circumferential microvessels are present in the PCD biomarker calculation. In these cases, Inf is replaced with the maximum finite value present in the feature vector, indicating a highly penetrating measure. By uniformly handling NaN and Inf values in this way, we ensure that the classification analysis remains unbiased and accurately reflects the data characteristics across all lesions. We investigated the robustness of the proposed postprocessing stage, as detailed in Supplementary File, Section S4. Low and consistent boundary line cases were observed for both univariable and multivariable analysis, except for the kurtosis biomarker.

Results

For illustrating the biomarkers obtained from the in vivo study, we have considered four subjects: two with benign and two with malignant lesions, encompassing both small and large lesion sizes. The four lesions, benign 1, benign 2, malignant 1, and malignant 2, were 7 mm, 25 mm, 8 mm, and 43 mm in size, respectively. In the B-mode image, the lesion is outlined in blue by the sonographer. The blue outline is then dilated by 2 mm and shown as the green border enclosing the actual lesion. Dilation makes a second boundary to include peritumoral vascularity, which is prominently seen in malignant tumors. It is noted that our technique uses the pattern of tumor microvessels for tumor classification, not the boundary features. The 2 mm dilation was empirically chosen, as our studies and previous research have shown that most peritumoral vasculature typically falls within this range from the tumor boundaries. Fig. 4 displays the B-mode image, HDMI microvessel image, and binarized polar coordinates for each lesion in the first three rows. The following rows of Fig. 4 present the values of all seven biomarkers: Histogram features, PGA, APD, PCD values, and illustrations of the ROI and central ROI for all four lesions. In the PGA section, the images display the lesion microvessel skeleton in red in the polar coordinates with their respective PGA values. In the APD section, the images show the binary image of the microvessels (in white) that are in contact with the ROI boundaries (depicted in grey) in Cartesian coordinates. The angle θ_i represents the computed angles for each microvessel segment (i) in contact with ROI, calculated using the APD algorithm. In the PCD row, each lesion is represented by four images. The top two images in the PCD section illustrate small microvessels oriented either circumferentially or penetrating the ROI. In contrast, the bottom row shows large microvessels with similar circumferential or penetrating orientations.

Correlation coefficients between pairs of the seven biomarkers, computed using Pearson correlation on all 70 breast masses in the in-vivo study, are presented in Fig. 5(h). The pairs of biomarkers that showed the highest correlation were MTH-MRH, and $kurtosis_r$ - $kurtosis_\theta$.

Box plots of all seven biomarkers, arranged in the decreasing order of statistical significance, are shown in Fig. 5(a)-(g). Among the seven biomarkers, five demonstrated significant differences between malignant and benign lesions. The median values for each biomarker of the benign and malignant cases are also shown in Fig. 5(a)-(g). The adjusted p-value, determined using the Holm-Šídák method, is displayed at the top of each subfigure.

Table 2 presents the AUC, SEN, and SPE [95% CIs] values for both the univariable model and multivariable models. The univariable model includes the seven biomarkers and BIRADS individually. The multivariable model has combination of multiple biomarkers like radial histogram features (MRH and $kurtosis_r$), tangential histogram features (MTH and $kurtosis_\theta$), polar coordinate features (MRH, $kurtosis_r$, MTH, $kurtosis_\theta$, and PGA), Cartesian coordinate features (APD and PCD), all seven biomarkers combined. Additionally, the model evaluates the combination of all seven biomarkers with BIRADS. Given the low number of

events per variable ($35/7 = 5$), there is a risk of optimism due to potential overfitting. To address this, a dimensional reduction approach based on PCA is applied to multivariable model analysis to reduce optimism in the models. PCA is performed on all seven biomarkers, and the first three principal components (PCs) are found to explain 97.3% of the total variation. Table 2 reports the performance of the model using three PCs alone and with the addition of BIRADS. The AUC obtained using three PCs is 0.91 [0.86, 0.97], while the AUC using three PCs plus BIRADS is 0.97 [0.91, 1.00]. Figure 6 presents the ROC plot for the univariable model, the multivariable model, and the multivariable model with PCA.

Discussion

This work introduces a new set of quantitative orientation-based microvessel biomarkers for tumor characterization: namely, MRH, $Kurtosis_r$, MTH, $Kurtosis_\theta$ PGA, APD, and PCD. The histogram features, MRH, MTH, $Kurtosis_r$ and $Kurtosis_\theta$ capture variations in the density and distribution of microvessels in polar-coordinate images. In the simulation study, cases with dominant circumferential microvessels exhibit a peakier radial histogram distribution than those with dominant penetrating microvessels. Specifically, case 1 (circumferential dominance) shows a higher Kurtosis_r value compared to cases 2, 3, 4, and 5. Although case 3 contains both penetrating and circumferential microvessels and may also exhibit a high Kurtosis_r, it can be distinguished from case 1 by its higher MRH (microvessel density) value. A similar trend is observed in the boxplot comparison between benign and malignant cases, where the median Kurtosis_r is higher for benign lesions. For tangential histograms, a reverse distribution is expected and is confirmed by the simulation study, where Kurtosis_Θ is higher in cases 2, 3, 4, and 5 compared to case 1. However, in vivo results deviate from this expectation, showing Kurtosis_Θ > Kurtosis_r, suggesting a predominantly penetrating vascular pattern often associated with malignancy. This discrepancy arises because benign lesions typically have sparse microvessel distributions, resulting in peaked histograms with high Kurtosis_Θ and Kurtosis_r values. In contrast, malignant lesions often exhibit both radial and tangential vessel orientations, leading to more uniform histograms with lower kurtosis values. Notably, some malignant lesions with high vessel density may contain more circumferential than penetrating microvessels, which can cause kurtosis-based interpretation to be misleading. In such cases, elevated MRH and MTH values aid in distinguishing malignant from benign lesions. Similarly, benign lesions may display small, discontinuous patterns within the ROI that appear penetrating in 2D imaging, resulting in high Kurtosis_Θ relative to Kurtosis_r, but are typically accompanied by low MRH and/or MTH. Therefore, Kurtosis_Θ is considered a valuable biomarker for differentiating benign from malignant lesions, particularly in cases with sparse microvessel distributions. Evidence supporting this argument can be found in the performance metrics. The tangential histogram (MTH with Kurtosis_Θ) demonstrates a higher sensitivity than MTH alone, with a similar trend observed for MRH and MRH with Kurtosis_r. These findings suggest that combining distributional information with density measures can improve classification performance. Another key observation is the high Pearson correlation coefficient between the biomarker pairs MTH–MRH and
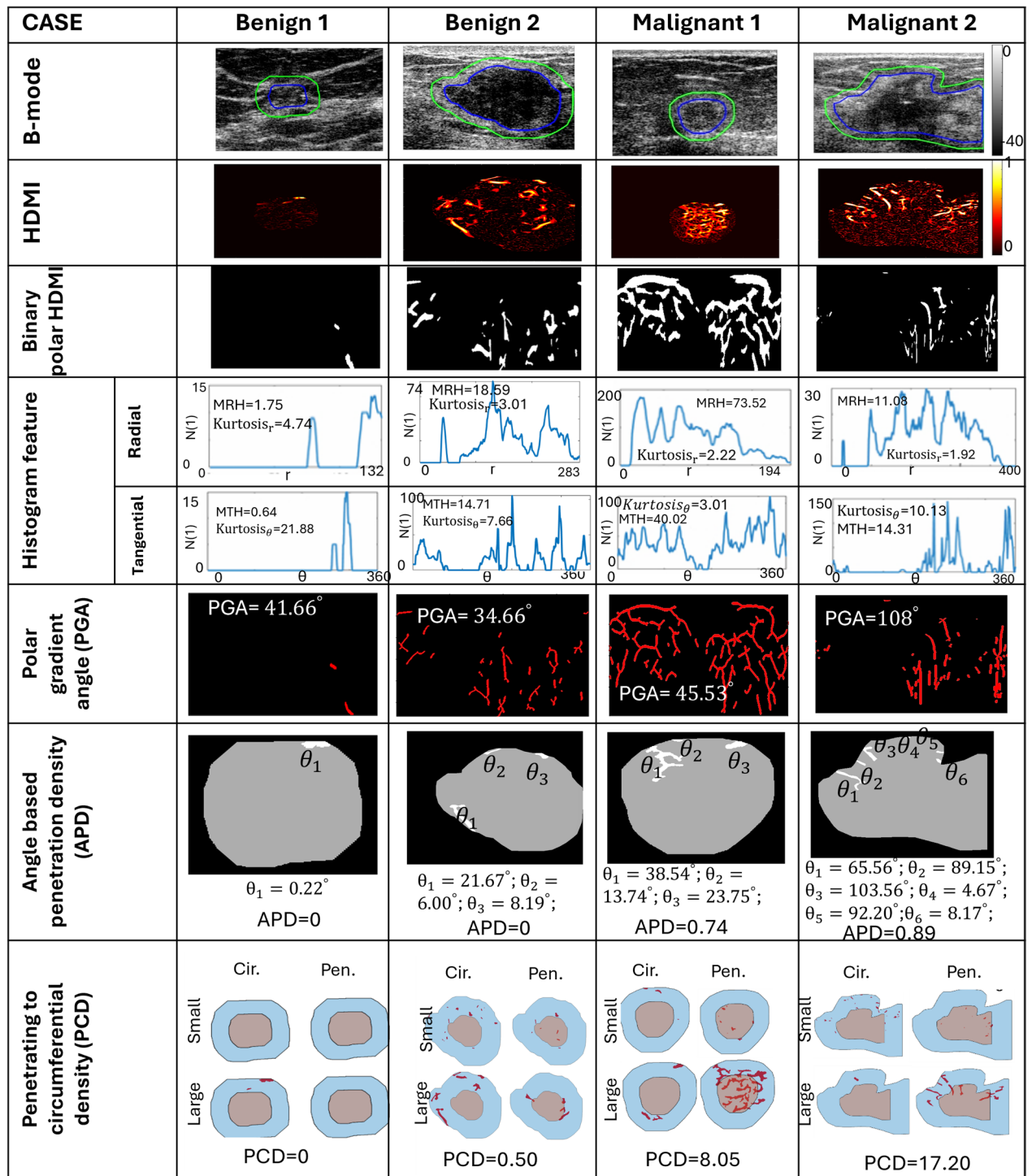
Fig. 4. Results of the in-vivo study for the selected benign and malignant samples. **Row 1**: lesion type. **Row 2**: B-mode image of each case with segmented ROI and dilation. **Row 3**: binary image of polar HDMI image. **Row 4**: radial and tangential histogram plots along with the biomarker values: MRH, kurtosis$_r$, MTH, and kurtosis$_\theta$. **Row 5**: skeleton of microvessel structure in polar coordinate along with PGA values. **Row 6**: microvessel structure in contact with lesion boundaries for each case, along with the value of angle (θ) of microvessel segments and APD. **Row** 7: small and large microvessel structure, characterized as circumferential and penetrating using the PCD approach along with the values of PCD.N(1): number of pixels having value of one.

Fig. 5. Box plots of all seven biomarkers and Pearson correlation coefficient plot. (**a**)-(**g**) Box plots of biomarkers MTH, MRH, APD, PCD, PGA, Kurtosis$_\Theta$ and Kurtosis$_r$. (**h**) The correlation coefficient plot between all seven biomarkers. p represent "Holm-Šidák" adjusted p-values, and the median values of distribution of benign and malignant case of each biomarker is also shown in the left side of each box plot. B = Benign and M = Malignant.

Kurtosis_Θ–Kurtosis_r. This is expected, as the mean parameters (MTH and MRH) both capture density-related information, while the kurtosis parameters (Kurtosis_Θ and Kurtosis_r) reflect the sparsity characteristics of the lesion.

The biomarker PGA quantifies the weighted mean of the gradient direction of the microvessel skeleton. Analysis indicates that PGA tends to be lower in benign lesions compared to malignant ones. Specifically, the median value of PGA for malignant cases is approximately 53° whereas it is 17° for benign cases. This difference arises because microvessels in benign lesions are predominantly circumferential, corresponding to horizontal orientation in polar coordinates. Ideally, the gradian angle in such cases approaches 0° when all microvessels are circumferential. In contrast, malignant lesions typically exhibit either a single penetrating microvessel or a combination of circumferential and penetrating microvessels with a higher density. This leads to both horizontal and vertical lines in polar coordinates, with an ideal gradient angle extending up to 180° when all microvessels are penetrating

The APD feature assesses whether the microvessels entering the ROI are penetrating toward the center of the ROI or are circumferential relative to the ROI. A microvessel is classified as penetrating if the angle θ (defined as the angle at which the ith microvessel enters the ROI boundary at the point of contact) falls within the range 30° to 150°. These angle limits were determined to be optimal for the current in vivo dataset through extensive testing with various thresholds. Simulation studies demonstrate that these biomarkers effectively discriminate penetrating microvessels from circumferential microvessels. Since malignant lesions often depend on feeding vessels, APD values are generally higher for malignant lesions compared to benign ones. This trend is consistently observed in our in vivo studies.

Biomarker	AUC [95% CI]	SEN [95% CI]	SPE [95% CI]
Univariable model			
MRH	0.88 [0.79, 0.95]	0.91 [0.69, 1.00]	0.77 [0.52, 1.00]
$kurtosis_r$	0.59 [0.44, 0.72]	0.66 [0.33, 1.00]	0.53 [0.11, 0.81]
MTH	0.92 [0.85, 0.97]	0.86 [0.44, 1.00]	0.78 [0.53, 1.00]
$kurtosis_\theta$	0.59 [0.45, 0.73]	0.87 [0.45, 1.00]	0.37 [0.14, 0.62]
PGA	0.75 [0.63, 0.85]	0.78 [0.35, 1.00]	0.58 [0.28, 0.85]
APD	0.81 [0.71, 0.91]	0.72 [0.50, 0.92]	0.91 [0.77, 1.00]
PCD	0.80 [0.69, 0.89]	0.71 [0.27, 1.00]	0.72 [0.33, 1.00]
BIRADS	0.78 [0.69, 0.85]	0.53 [0.30, 0.77]	0.97 [0.88, 1.00]
Multivariable model			
Radial histogram feature (MRH and $kurtosis_r$)	0.86 [0.79, 0.96]	0.93 [0.85, 1.00]	0.73 [0.59, 0.88]
Tangential histogram features (MTH and $kurtosis_\theta$)	0.93 [0.86, 1.00]	0.93 [0.86, 1.00]	0.76 [0.61, 0.90]
Polar coordinate features (MRH. $kurtosis_r$, MTH and $kurtosis_\theta$, and PGA)	0.92 [0.86, 0.97]	0.92 [0.84, 1.00]	0.81 [0.72, 0.99]
Cartesian coordinate feature (APD and PCD)	0.92 [0.87, 0.98]	0.92 [0.84, 1.00]	0.79 [0.69, 0.96]
All seven combined	0.94 [0.84, 0.99]	0.88 [0.81, 1.00]	0.90 [0.88, 1.00]
All seven combined + BIRADS	0.96 [0.90, 1.00]	0.94 [0.89, 1.00]	0.94 [0.94, 1.00]
Multivariable with PCA			
3 PCs	0.91 [0.86, 0.97]	0.93 [0.84, 1.00]	0.77 [0.65, 0.94]
3 PCs + BIRADS	0.97 [0.91, 1.00]	0.95 [0.89, 1.00]	0.88 [0.81, 1.00]

Table 2. Performance measure of univariable model and multivariable model.
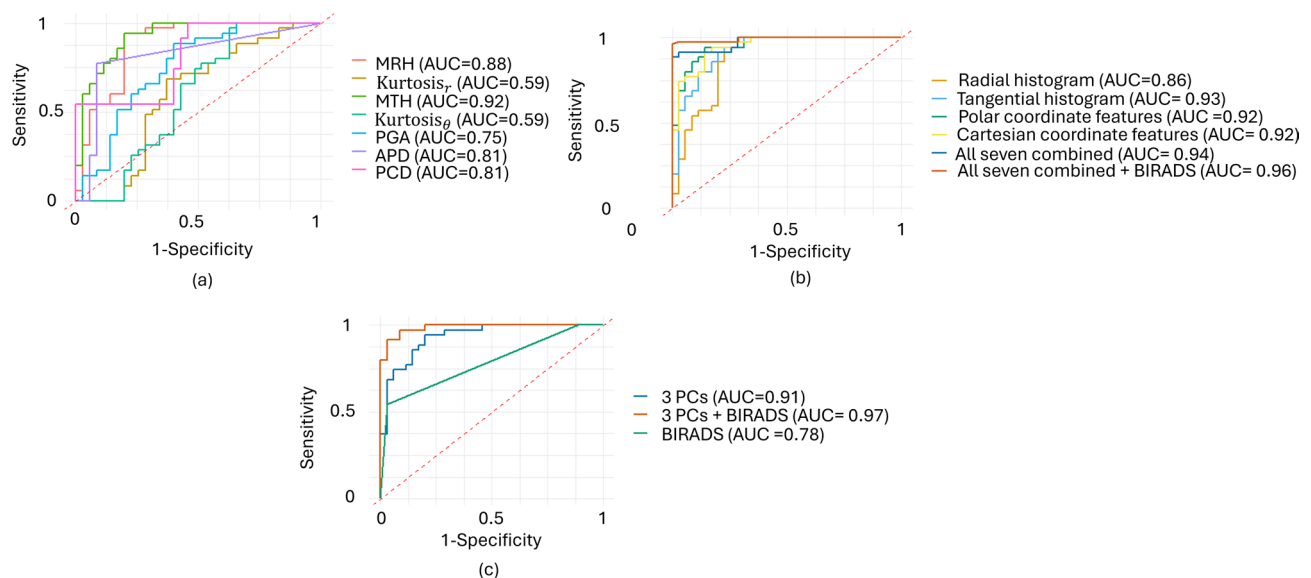

Fig. 6. ROC plots. (**a**) Univariable model, (**b**) Multivariable model, and (**c**) Multivariable PCA model.

PCD measures the ratio of the area of penetrating microvessels to the area of circumferential microvessels, with the distribution expected to follow a pattern similar to APD. However, the low correlation between the two suggests that they reflect different aspects of the vascular pattern. While PCD focuses on the proportion of vessels approaching the lesion center, APD is based on the entry angle of vessels at the ROI boundary. Notably, APD excludes vessels that do not contact the ROI boundary, which may happen if portions of the vessel fall outside the imaging plane. When used in combination, APD and PCD provide complementary information, offering improved classification performance over either metric alone.

Combining all seven biomarkers demonstrated performance compared to BIRADS alone, as shown in the ROC plots. However, the multivariable model is prone to optimism bias due to a low events per variable ratio. To address this, dimensionality reduction was performed using PCA, and the first three PCS were used for

classification. The multivariable model based on three PCs also outperformed BIRADS alone. Furthermore, incorporating BIRADS alongside the proposed biomarkers and three PCs resulted in an additional improvement in classification performance. Although using PCA features improves the performance, it affects the interpretability of biomarkers, which is crucial for clinical practice. A hybrid approach that includes both PCA-derived features and proposed biomarkers, could balance model performance and interpretability in clinical applications. Additionally, since the main reason behind choosing PCA is a low sample size, it would be valuable to evaluate multi-variable classification performance on a larger dataset.

Notably, the proposed approach correctly classified a benign lesion with high vascularity ('benign 2' in Fig. 4), despite its MRH and MTH values being comparable to those of a malignant lesion ('malignant 2'). While high vascularity often suggests malignancy, the model accurately identified this case as benign, demonstrating its ability to distinguish between lesion types with overlapping vascular features. Further analysis with a larger sample of highly vascular lesions is needed to better define the method's limits and confirm its robustness.

Raza et al.[6] were the first to investigate microvessel orientation for classifying benign and malignant cases, drawing inspiration from previous research findings[34–36] suggesting the association of penetrating microvessels and disorderly branching pattern in malignant lesions. Through visual inspection of color Doppler images, investigators found a connection between penetrating microvessels and malignancy, achieving a performance of SEN = 0.68 and SPE = 0.95 [6]. Subsequent studies have also explored this salient feature[8,37–39] reporting sensitivity ranges from 0.56 to 0.76 and specificity ranges from 0.72 to 0.95. While some performance results are close to our findings, the risk of misclassification and inherent subjectivity associated with using color Doppler remains significant. This limitation arises from reliance on visual inspection by different experts, introducing the potential for interobserver variability. Their studies also have limitations, as they employed conventional color Doppler techniques, which lack the sufficient sensitivity required to visualize microvessels effectively[40,41]. The utility of conventional color Doppler techniques in diagnosing breast cancer remains controversial and was excluded from the Breast Imaging Reporting and Data System (BI-RADS) categorization of the American College of Radiology[42,43]. While some research groups continue to investigate the potential role of color Doppler, no definitive conclusions have been reached to date[42].

The proposed orientation-based biomarkers were evaluated using 2D HDMI, which ignores orientation properties in the 3D space. This aspect opens opportunities for future research to explore and expand applications by incorporating 3D spatial analysis from volumetric images. For example, the histogram feature currently computes the distribution of microvessels relative to the center of the ROI in 2D, which does not accurately represent the true distribution of microvessels in a 3D ROI. Volumetric evaluation of orientation-based biomarkers requires 3D HDMI[44] for extraction of 3D biomarkers. Additionally, as the proposed biomarkers use pixel-based thresholding to characterize small and large microvessels, future research could explore adaptive threshold strategies tailored to different sizes. Further, alternative optimization algorithms for microvessel fitting may improve accuracy. The relatively small sample size in the current study limited precision of biomarker estimates and multivariable model performance metrics. Future research using larger datasets is warranted to further validate our findings.

Another area for future studies would be to integrate the orientation-based biomarkers with the previously proposed morphological biomarkers of microvessels[20,21] to further enhance the diagnostic performance. In addition to diagnostic applications, the biomarkers presented in this paper hold potential for monitoring response to neoadjuvant therapy in breast cancer patients. Furthermore, the proposed biomarker could also be adapted for cancer diagnosis in other anatomical sites.

Conclusion

This work presents novel quantitative methods for characterizing microvasculature orientation-based microvasculature biomarkers derived from a non-contrast-enhanced ultrasound technique, HDMI. The newly developed orientation-based biomarkers, MRH, Kurtosis_r, MTH, Kurtosis_Θ PGA, APD, and PCD demonstrated effectiveness in classifying breast masses. These findings suggest that the proposed orientation-based biomarkers derived from HDMI provide additional quantitative diagnostic information and can serve as a complementary tool to aid cancer diagnosis. In conclusion, this study is an important initial step toward developing a framework for lesion classification using HDMI-derived orientation biomarkers. While the findings are promising, further validation with larger datasets is necessary before clinical translation can be realized.

Data availability

The datasets used and/or analyzed during the current study are available from the corresponding author on reasonable request.

Code availability

The custom code or mathematical algorithms that are deemed central to the conclusions are available from the corresponding author upon request.

References

1. Nakamura, Y. et al. Flt-4-Positive vessel density correlates with vascular endothelial growth Factor-D expression, nodal status, and prognosis in breast Cancer. *Clin. Cancer Res.* **9**, 5313–5317 (2003).
2. Longatto Filho, A., Lopes, J. M. & Schmitt, F. C. Angiogenesis and breast cancer. *J. Oncol.* 576384 (2010). (2010).

3. Carmeliet, P. & Jain, R. K. Angiogenesis in cancer and other diseases. *Nature* **407**, 249–257 (2000).
4. Nagy, J. A., Chang, S. H., Dvorak, A. M. & Dvorak, H. F. Why are tumour blood vessels abnormal and why is it important to know? *Br. J. Cancer.* **100**, 865–869 (2009).
5. Ibrahim, R. et al. Evaluation of solid breast lesions with power doppler: value of penetrating vessels as a predictor of malignancy. *Singap. Med. J.* **57**, 634–640 (2016).
6. Raza, S. & Baum, J. K. Solid breast lesions: evaluation with power doppler US. *Radiology* **203**, 164–168 (1997).
7. Busilacchi, P., Draghi, F., Preda, L. & Ferranti, C. Has color doppler a role in the evaluation of mammary lesions? *J. Ultrasound.* **15**, 93–98 (2012).
8. Lee, S. W., Choi, H. Y., Baek, S. Y. & Lim, S. M. Role of color and power doppler imaging in differentiating between malignant and benign solid breast masses. *J. Clin. Ultrasound JCU.* **30**, 459–464 (2002).
9. Lee, S. C. et al. Contrast-Enhanced ultrasound imaging of breast masses: adjunct tool to decrease the number of False-Positive biopsy results. *J. Ultrasound Med. Off J. Am. Inst. Ultrasound Med.* **38**, 2259–2273 (2019).
10. Du, Y. R., Wu, Y., Chen, M. & Gu, X. G. Application of contrast-enhanced ultrasound in the diagnosis of small breast lesions. *Clin. Hemorheol Microcirc.* **70**, 291–300 (2018).
11. Gessner, R. C., Frederick, C. B., Foster, F. S. & Dayton, P. A. Acoustic angiography: a new imaging modality for assessing microvasculature architecture. *Int. J. Biomed. Imaging* 936593 (2013). (2013).
12. Errico, C. et al. Ultrafast ultrasound localization microscopy for deep super-resolution vascular imaging. *Nature* **527**, 499–502 (2015).
13. Opacic, T. et al. Motion model ultrasound localization microscopy for preclinical and clinical multiparametric tumor characterization. *Nat. Commun.* **9**, 1527 (2018).
14. Shelton, S. E., Stone, J., Gao, F., Zeng, D. & Dayton, P. A. Microvascular ultrasonic imaging of angiogenesis identifies tumors in a murine spontaneous breast cancer model. *Int. J. Biomed. Imaging* 7862089 (2020). (2020).
15. Christensen-Jeffries, K. et al. Super-resolution ultrasound imaging. *Ultrasound Med. Biol.* **46**, 865–891 (2020).
16. Demené, C. et al. Spatiotemporal clutter filtering of ultrafast ultrasound data highly increases doppler and fUltrasound sensitivity. *IEEE Trans. Med. Imaging.* **34**, 2271–2285 (2015).
17. Bercoff, J. et al. Ultrafast compound doppler imaging: providing full blood flow characterization. *IEEE Trans. Ultrason. Ferroelectr. Freq. Control.* **58**, 134–147 (2011).
18. Bayat, M., Fatemi, M. & Alizad, A. Background removal and vessel filtering of Noncontrast ultrasound images of microvasculature. *IEEE Trans. Biomed. Eng.* **66**, 831–842 (2019).
19. Xiao, X. Y. et al. Superb microvascular imaging in diagnosis of breast lesions: a comparative study with contrast-enhanced ultrasonographic microvascular imaging. *Br. J. Radiol.* **89**, 20160546 (2016).
20. Ternifi, R. et al. Quantitative biomarkers for Cancer detection using Contrast-Free ultrasound High-Definition microvessel imaging: fractal dimension, murray's deviation, bifurcation angle & Spatial vascularity pattern. *IEEE Trans. Med. Imaging.* **40**, 3891–3900 (2021).
21. Ghavami, S., Bayat, M., Fatemi, M. & Alizad, A. Quantification of morphological features in non-contrast-enhanced ultrasound microvasculature imaging. *IEEE Access. Pract. Innov. Open. Solut.* **8**, 18925–18937 (2020).
22. Ternifi, R. et al. Ultrasound high-definition microvasculature imaging with novel quantitative biomarkers improves breast cancer detection accuracy. *Eur. Radiol.* **32**, 7448–7462 (2022).
23. Kurti, M. et al. Quantitative biomarkers derived from a novel contrast-free ultrasound high-definition microvessel imaging for distinguishing thyroid nodules. *Cancers* **15**, 1888 (2023).
24. Sabeti, S. et al. Morphometric analysis of tumor microvessels for detection of hepatocellular carcinoma using contrast-free ultrasound imaging: A feasibility study. *Front Oncol* **13**, (2023).
25. Ferroni, G. et al. Noninvasive prediction of axillary lymph node breast cancer metastasis using morphometric analysis of nodal tumor microvessels in a contrast-free ultrasound approach. *Breast Cancer Res.* **25**, 65 (2023).
26. Adusei, S. A. et al. Quantitative biomarkers derived from a novel, Contrast-Free ultrasound, High-Definition microvessel imaging for differentiating choroidal tumors. *Cancers* **16**, 395 (2024).
27. Park, A. Y. & Seo, B. K. Up-to-date doppler techniques for breast tumor vascularity: Superb microvascular imaging and contrast-enhanced ultrasound. *Ultrason. Seoul Korea.* **37**, 98–106 (2018).
28. Jung, H. K., Park, A. Y., Ko, K. H. & Koh, J. Comparison of the diagnostic performance of power doppler ultrasound and a new microvascular doppler ultrasound technique (AngioPLUS) for differentiating benign and malignant breast masses. *J. Ultrasound Med. Off J. Am. Inst. Ultrasound Med.* **37**, 2689–2698 (2018).
29. Weind, K. L., Maier, C. F., Rutt, B. K. & Moussa, M. Invasive carcinomas and fibroadenomas of the breast: comparison of microvessel distributions–implications for imaging modalities. *Radiology* **208**, 477–483 (1998).
30. Mohindra, N. et al. Utility of ultrasound Angio-PLUS imaging for detecting blood flow in breast masses and comparison with color doppler for differentiating benign from malignant masses. *Acta Radiol.* **64**, 2087–2095 (2023).
31. Lam, L., Lee, S. W. & Suen, C. Y. Thinning methodologies-a comprehensive survey. *IEEE Trans. Pattern Anal. Mach. Intell.* **14**, 869–885 (1992).
32. Regionprops. https://www.mathworks.com/help/images/ref/regionprops.html
33. DeCarlo, L. T. On the meaning and use of kurtosis. *Psychol. Methods.* **2**, 292–307 (1997).
34. Schor, A. M. & Schor, S. L. Tumour angiogenesis. *J. Pathol.* **141**, 385–413 (1983).
35. Folkman, J. & Klagsbrun, M. *Angiogenic Factors Science* **235**, 442–447 (1987).
36. Folkman, J., Merler, E., Abernathy, C. & Williams, G. Isolation of a tumor factor responsible for angiogenesis. *J. Exp. Med.* **133**, 275–288 (1971).
37. Jung, H. K., Park, A. Y., Ko, K. H. & Koh, J. Comparison of the diagnostic performance of power doppler ultrasound and a new microvascular doppler ultrasound technique (AngioPLUS) for differentiating benign and malignant breast masses. *J. Ultrasound Med.* **37**, 2689–2698 (2018).
38. Svensson, W. E., Pandian, A. J. & Hashimoto, H. The use of breast ultrasound color doppler vascular pattern morphology improves diagnostic sensitivity with minimal change in specificity. *Ultraschall Med. Stuttg Ger. 1980.* **31**, 466–474 (2010).
39. Kook, S. H. et al. Evaluation of solid breast lesions with power doppler sonography. *J. Clin. Ultrasound.* **27**, 231–237 (1999).
40. Birdwell, R. L., Ikeda, D. M., Jeffrey, S. S. & Jeffrey, R. B. Preliminary experience with power doppler imaging of solid breast masses. *AJR Am. J. Roentgenol.* **169**, 703–707 (1997).
41. Leek, R. D., Landers, R. J. 2, Harris, A. L. & Lewis, C. E. Necrosis correlates with high vascular density and focal macrophage infiltration in invasive carcinoma of the breast. *Br. J. Cancer.* **79**, 991–995 (1999).
42. Watanabe, T. et al. Multicenter prospective study of color doppler ultrasound for breast masses: utility of our color doppler method. *Ultrasound Med. Biol.* **45**, 1367–1379 (2019).
43. Breast Imaging Reporting & Data System. https://www.acr.org/Clinical-Resources/Reporting-and-Data-Systems/Bi-Rads
44. Gu, J. et al. Volumetric imaging and morphometric analysis of breast tumor angiogenesis using a new contrast-free ultrasound technique: a feasibility study. *Breast Cancer Res.* **24**, 85 (2022).

Author contributions

A.A: Conceptualization & design, Methodology, Investigation, Visualization, Interpretation, Validation, Ad-

ministrative, Resources, Funding, Supervision, Critical review, and Editing. M.F.: Conceptualization & design, Methodology, Investigation, Visualization, Interpretation, Validation, Administrative, Resources, Funding, Supervision, Critical review and editing. P. K. C.: Visualization, Interpretation, Investigation, Statistical analysis, Validation, Writing the original draft, Critical review and Editing N.B. L.: Statistical methods, Formal analysis, Critical review, and Editing.

Funding

Declarations

Competing interests

The authors declare no competing interests.

Ethics approval

The Research involved human participants. The study received institutional review board approval (IRB#: 19-003028) and was Health Insurance Portability and Accountability Act (HIPAA) compliant. All procedures performed in this study were in accordance with the ethical standards of the institutional and/or national research committee and with the 1964 Helsinki declaration and its later amendments or comparable ethical standards.

Informed consent

Signed IRB-approved informed consent with permission for publication was obtained from all individual participants included in the study.

Additional information

Supplementary Information The online version contains supplementary material available at https://doi.org/10.1038/s41598-025-09745-x.

Correspondence and requests for materials should be addressed to A.A. or M.F.

Reprints and permissions information is available at www.nature.com/reprints.

Publisher's note Springer Nature remains neutral with regard to jurisdictional claims in published maps and institutional affiliations.